

Supplemental Information – Hysteresis and Hydrodynamic Collapse in Leidenfrost Vapor Layers

Dana Harvey, Joshua Méndez Harper, and Justin C. Burton*
Department of Physics, Emory University, Atlanta, Georgia 30322, USA

I. SUPPLEMENTARY VIDEOS

Video S1: A machined aluminum block with a concave, spherical surface is heated with an embedded ceramic heater, and the temperature is measured with a thermocouple. Pure DI water is periodically dropped onto the surface with a syringe to determine if the surface is hot enough to spontaneously form a vapor layer beneath the drop. A stable drop is formed at $T_+ \approx 212^\circ\text{C}$. The aluminum is then allowed to cool. The drop evaporates and remains levitating until the block temperature is below boiling (100°C).

Video S2: The rounded tip of a nickel-plated copper rod is immersed in a bath of DI water at 75°C . The metal is heated using an embedded ceramic heater with an internal thermocouple. When the metal reaches $T_+ \approx 260^\circ\text{C}$ a stable vapor layer is formed. Upon cooling, the vapor layer exists until the metal reaches $T_- \approx 140^\circ\text{C}$.

Video S3: High-speed video showing the collapse of a vapor layer at a surface temperature $T_s = T_-$. The original video was recorded at 33,000 fps, and the playback rate is 1,650 times slower than real time. A single failure point results in a wetting front that travels at the capillary velocity ($\gamma/\eta_w \approx 210$ m/s), followed by nucleate boiling.

Video S4: Results from a two-dimensional simulation in COMSOL [1] employing heat transfer, laminar flow, and phase field modules to model the Leidenfrost vapor layer around a heated semicircle in water. The profile here shows the water (blue) and vapor (white) phases of water as the system cools. We chose the 80% vapor phase line to delineate the phases in the video. The vapor layer collapses ≈ 43 s after formation at an average surface temperature of $T_s \approx 190^\circ\text{C}$.

II. EXPERIMENTAL APPARATUS

Our experimental Leidenfrost system was designed for high-speed measurements of the dynamics of the vapor layer. The apparatus consisted of metal rods with hemispherical tips immersed in a bath of water with an adjustable salt concentration (Fig. 1b in the main text).

We controlled the height of the water bath, H , the temperature of the bath, T_l , the temperature of the rod, T_s , and the position of the rod in the bath. H and T_l were controlled using an exterior water bath. The exterior water bath rests on a hot plate so that $T_l \approx 75^\circ\text{C}$. The bath was connected by a small tube to the experiment so that water could be gravitationally siphoned in order to keep H constant. We also used silicon heaters glued to the experimental chamber to keep the water temperature consistent. T_l was measured using a k-type thermocouple immersed in the bath.

The upper metal electrodes used in the experiment were cylinders of length 8.90 cm and radii 7.94 mm. They were constructed from titanium alloy, brass, and copper. The brass and copper were electroplated with nickel to resist corrosion. At one end there was a hemispherical tip with radius 7.94 mm, and at the other end was a lip of radius 1.11 cm. The lip held the electrode in place and housed electrical connections to the BNC cables. The lip rested on ceramic, insulating washers attached to a vertical, linear motion system in order to move the electrode up and down. The lower electrode, same geometry, but 6.35 cm long, was fully immersed in the bath and machined from titanium alloy so that it was resistant to salt water (Fig. 1b in the main text). The electrodes were heated using a cylindrical ceramic heater that was cemented in the center of the rod. A K-type thermocouple at the end of the ceramic heater measured T_s near the tip.

Fig. S1 shows a schematic of the measurement system, including the RG58C/U cables, which are important for correctly interpreting the electrical impedance of the Leidenfrost system. Z_{unknown} represents the complex impedance of the Leidenfrost system (Fig. 1c in the main text), including any parasitic capacitance or inductance. During measurements, a sinusoidal carrier signal with frequency $f = 10$ MHz and variable amplitude = 0.2-3.5 V is generated by an Agilent 33220A function generator. The signal is split into two cables of identical length ($L1$), and passed through both Z_{unknown} and a 6 dB pi-pad attenuator before being acquired by two channels of a National Instruments PCI-5153 computer-based oscilloscope. The attenuator minimizes noise of the final measurement by forcing the voltage range of each channel to be the same [2]. Since the impedance of both channels and the attenuator was 50Ω , only reflections above Z_{unknown} were considered in the model.

While we use the same carrier wave frequency for all experiments, we sample the data differently. For short time scales, we used a sample rate of 200 MS/s for 50 ms of data, for a total of 10 MS (here “MS” refers to “megasamples”). This is equivalent to 20 sampled points

* justin.c.burton@emory.edu

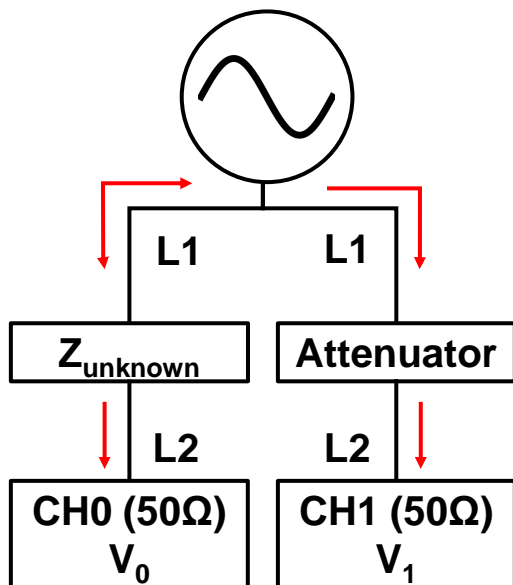


FIG. S1. Measurement system used to determine Z_{unknown} of the Leidenfrost system. The carrier wave (10 MHz) traveled along RG58C/U cables of lengths $L1$ and $L2$. The telegraphers equations are solved along each length of cable. Arrows indicate allowed directions of current along each cable. By simultaneously measuring V_0 and V_1 , we could determine Z_{unknown} .

per cycle for the 10 MHz carrier wave. We wrote a custom LabVIEW program that acts as a lock-in amplifier to extract the 10 MHz amplitude for each cycle, resulting in a total of 500,000 data points for the data shown in Fig. 2 (main text) and S3. For some experiments, such as those shown in Figs. 1 and 3 in the main text, the thickness d_c is measured over many minutes. For these measurements, we averaged 800 samples at 100 MS/s to calculate the thickness of the vapor layer in 1 s intervals. Additionally, T_s and T_l were also measured every second.

III. ELECTRICAL MEASUREMENTS OF THE VAPOR LAYER

In order to measure Z_{unknown} , and ultimately the thickness of the vapor layer, we solved the telegraphers equations on each cable, and matched the boundary conditions at Z_{unknown} and the attenuator (Fig S1). We ignored losses and assumed a capacitance, C_c , and inductance, L_c , per unit length of cable. Along the length x of each cable, the voltage V and current I are determined by:

$$\frac{dV}{dx} = -L_c \frac{dI}{dt}, \quad (1)$$

$$\frac{dI}{dx} = -C_c \frac{dV}{dt}. \quad (2)$$

Assuming a plane wave ansatz, $V = V_c e^{i(k_c x - \omega t)}$ and $I = V/\sqrt{L_c/C_c}$, where V_c is the amplitude, k_c is the wave vector, and $\omega = 2\pi f$ is the angular frequency, we solve for the real and imaginary components of Z_{unknown} , Z_R and Z_I , respectively.

By taking the real part of the signals, the resulting expressions for Z_R and Z_I can be written in terms of the measured signals (CH0 and CH1, Fig. S1). For each channel, the voltage can be written as a sum of sine and cosine:

$$V_0 = A_0 \cos \omega t + B_0 \sin \omega t \quad (3)$$

$$V_1 = A_1 \cos \omega t + B_1 \sin \omega t. \quad (4)$$

The LabVIEW program extracts A_0 , A_1 , B_0 , and B_1 for each cycle of oscillation of the 10 MHz carrier wave. Thus, the amplitudes are sampled every 100 ns. Z_R and Z_I are then computed using the following relations:

$$Z_R = \frac{-R_{\text{in}}}{A_0^2 + B_0^2} \left(A_0^2 - A_0 A_1 A_F + B_0 (B_0 - A_F B_1) \right) \quad (5)$$

$$+ A_F (A_1 B_0 - A_0 B_1) \tan \left(\frac{L\omega}{v} \right),$$

$$Z_I = \frac{R_{\text{in}}}{A_0^2 + B_0^2} \left(-A_1 A_F B_0 + A_0 A_F B_1 + \quad (6)$$

$$(A_0^2 - A_0 A_1 A_F + B_0 (B_0 - A_F B_1)) \tan \left(\frac{L\omega}{v} \right) \right).$$

where $R_{\text{in}} = 50 \Omega$ is the input impedance of the oscilloscope channels, $L = L1 = 1.1$ m is the measured length of L1, $v = 0.65c$ is the wave speed on the cable (relative to the speed of light c), and $A_F = 2.02$ is the measured voltage attenuation ratio for the 6 dB attenuator.

Ultimately we want to relate Z_R and Z_I to R_0 , C_v , and C_λ , as shown in Fig. 1c in the main text. In the circuit diagram, we have ignored any geometric capacitance associated with the electrodes, since our measurements suggest these are less than 0.2 pF, while both C_v and C_λ are always greater than ≈ 30 pF. Since C_v and C_λ are summed in parallel, we can only measure the total capacitance $C_v + C_\lambda$ (Fig. 1c, Fig. S2). Thus, R_0 and $C_v + C_\lambda$ can be written as:

$$R_0 = Z_R, \quad (7)$$

$$C_v + C_\lambda = \frac{1}{\omega(Z_I + L_0\omega)}. \quad (8)$$

$C_v + C_\lambda$ and R_0 are functions of time. However, we must determine the value of L_0 . This is a parasitic reactance that is in series with the other components. In order to measure L_0 in the experiments, we use the fact that the impedance associated with C_λ is almost negligible when there is a fully-formed double layer. The length scale associated with charge separation is $\lambda \approx 1 - 10$ nm [3], which is more than 3 orders of magnitude smaller than the typical vapor layer thickness d (Fig. S2). Prior to collapse, there is no liquid-solid contact so $C_\lambda = 0$.

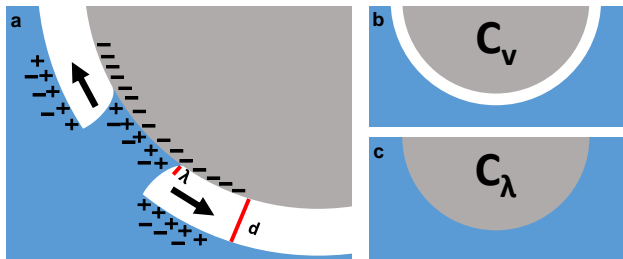


FIG. S2. (a) During the collapse of a vapor layer with thickness d , the capacitance rapidly changes due to the formation of a double layer of thickness $\lambda \ll d$. (b) Prior to collapse, the capacitance is solely determined by the capacitance of the vapor layer, C_v . (c) After collapse, it is the double layer capacitance, C_λ , which dominates the parallel combination.

Well after collapse, when there is significant liquid-solid contact, $C_v = 0$ and $C_\lambda > 1 \mu\text{F}$ for the centimeter-scale electrodes in our experiment [3]. At $f = \omega/2\pi = 10$ MHz, the corresponding impedance is $1/|\omega C_\lambda| \approx 0.016 \Omega$. Thus, we can ignore the impedance due to C_λ and assume $L_0 = iZ_I/\omega$ when there is a double layer. For our experiments, $L_0 \lesssim 1 \mu\text{H}$. We then use this measured value of L_0 for each experiment and apply it to data before, during, and after the collapse.

The time evolution of the impedances R_0 and $1/\omega(C_v + C_\lambda)$ for a typical experiment are shown in Fig. S3. The vapor layer collapses by the propagation of a wetting front at ≈ 25 ms, followed by an explosion of bubbles (Video S3). Prior to collapse, the resistance is mostly due to the bulk ions in the water, and there is no liquid-solid contact, so $C_\lambda = 0$. Capillary waves are easily observed in the capacitive reactance before collapse. 30 s after collapse, when the system is quiescent and bubbles have dissipated, R_0 returns nearly to the initial starting value, although slightly less. We attribute this to the heat delivered to the water during collapse, which reduces the viscosity, and correspondingly, the bulk resistivity. Since we have attributed the remaining reactance to L_0 , as described above, the capacitive reactance is near zero 30 s after collapse.

During the collapse and the following explosion of bubbles, both impedances vary significantly (Fig. S3, insets). It is difficult to interpret the data here since the flow in the water likely influences the formation dynamics of the double layer, and advects charge with the flow. The initial drop in the capacitive impedance (Fig. S3b, inset) is due to the rapid increase in capacitance from the liquid solid contact (Fig. 2b). Then the vapor layer explodes and collapses again, resulting in two distinct peaks in R_0 , and negative values of $C_v + C_\lambda$. We do not expect our simple circuit model to accurately represent the complex physics in this regime.

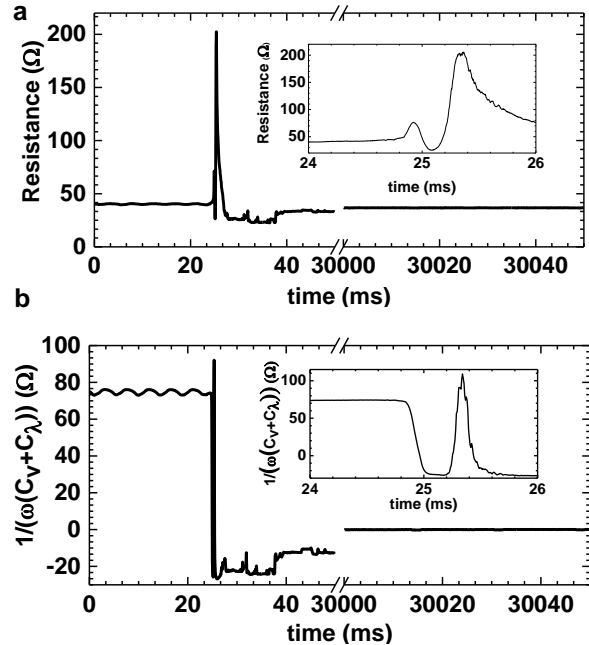


FIG. S3. Resistance (a) and capacitive reactance (b) of the Leidenfrost cell during collapse with 0.02 M NaCl. The insets show 2 ms of the data right before and after collapse. The wetting front begins spreading at ≈ 25 ms (Video S3). 30 s after collapse, the system is quiescent. During collapse, the rapid evaporation and bubble nucleation leads to large variations in the data, as described in the text.

IV. COMPUTING THE VAPOR LAYER THICKNESS

Prior to collapse, we calculate the average vapor layer thickness from the capacitance measurements. We start with the assumption that our system can be modeled by concentric hemispheres (Fig. S4). The leading-order equation for capacitance is then:

$$C_v = 2\pi\epsilon_v \frac{R(R+d)}{d}, \quad (9)$$

where $R = 7.9$ mm is the radius of the spherical tip, d is the vapor layer thickness, and $\epsilon_v = 1.0057\epsilon_0$ is the dielectric constant of water vapor at 100°C . The water level H was sometimes lower (or higher) such that the hemispherical capacitor model needed to be amended. We monitored H in corresponding videos of experiments to measure changes in time. To account for changes in H below the full hemisphere, we multiplied Eq. 9 by H/R , which gives the exact fractional area of the hemisphere immersed in the water. We also multiply by a small correction factor of order unity, c , which was derived from detailed modeling.

The resulting expression for C_v is:

$$C_v = 2\pi c H \epsilon_v \frac{R+d}{d}. \quad (10)$$

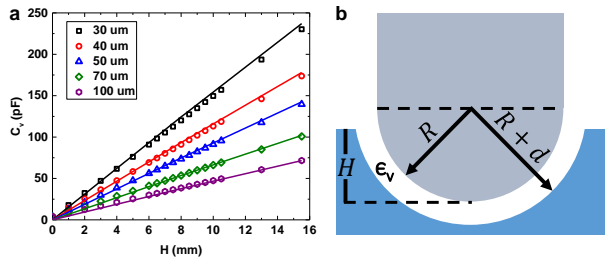


FIG. S4. (a) Data from the COMSOL model showing the geometric capacitance of the vapor layer. The data is plotted as a function of H , and different symbols and colors correspond to different values of the gap thickness d . The solid lines represent fits using eq. 10 with $c = 1.051$. (b) Simplified geometry for modeling the capacitance of the vapor layer.

To calculate thickness of the vapor layer, we solve for d :

$$d = R \left(\frac{C_v}{2\pi c H \epsilon_v} - 1 \right)^{-1}. \quad (11)$$

In order to verify this approximation and compute the constant c , we modeled our geometry and computed the capacitance in COMSOL [1]. The model consisted of a three-dimensional conductive cylinder with a hemispherical tip immersed a distance H in a conducting half-space. A small shell of material of thickness d was removed from the half space, as shown in Fig. S4b. We then used the electrostatic module in COMSOL. This module essentially solves Laplace's equation for the electrostatic potential, given the conducting boundary conditions. One electrode has the same geometry of the heated rods in our experiment, and the other is the surface of the water. The two objects are separated by a vacuum.

The simulation was bounded by a cylinder of the same size as our experimental system (height = 15 cm and radius = 7 cm). The upper electrode was a cylinder of radius $R = 7.9$ mm and height = 6.5 cm with a hemisphere tip of $R = 7.9$ mm. The cylinder is centered in the container with its flat end at the top. The second electrode represents the water surface. We varied the thickness of the vapor layer, d , and the water height, H , when computing the capacitance. Figure. S4a shows the resulting capacitance from the simulation when varying d from 30-100 μm and H from 0-1.5mm, so that the water level actual surpasses the hemispherical tip. In experiments, H varied from 0.1-7.9 mm. The solid lines in Fig. S4a are fits to the data using Eq. 11 with $c = 1.051$. The agreement is very good. With this additional correction, Eq. 11 is a reliable and quantitative way to extract d from measurements of C_v .

V. HYSTERESIS EXPERIMENTS

As shown in Fig. 1d in the main text, the temperature at which the vapor layer forms (T_+) is much higher than

the temperature at which it eventually collapses (T_-). To measure this hysteresis, the upper metal electrode was immersed into the bath before heating. The initial temperature of the bath was set at $T_i = 75^\circ\text{C}$. We used the nickel plated copper rod and pure DI water. Salt was not added so as to avoid deposition of salt on the surface during the nucleate boiling regime while heating. The upper electrode was then heated until a stable vapor layer formed when $T_s \approx T_+$ (Video S2).

We measured d , T_s , and T_i every second. For all experiments, we sampled the 10 MHz signal at 100 MS/s and averaged 800 cycles every second to form one data point. After the vapor layer formed, the heater was turned off and the rod was allowed to cool. Eventually, at a lower temperature T_- , the vapor layer failed and violent boiling ensued. We found that on average, $T_- \approx 140^\circ\text{C}$ and $T_+ \approx 260^\circ\text{C}$. For nearly all experiments, we maintain a water height $H \approx R$, but we note that the water height plays a significant role in the exact value of T_- since it controls the hydrostatic pressure gradient on the vapor layer. Larger values of H increased T_- , and smaller values of H decreased T_- .

We observed similar hysteresis in Leidenfrost drops. In these experiments, we used an aluminum substrate with a concave polished surface. The substrate is heated with an embedded ceramic heater. A k-type thermocouple read the temperature of the aluminum near the drop. Water was periodically dropped on the surface until a vapor layer formed instantaneously at $T_+ \approx 212^\circ\text{C}$. The heater was then turned off and the aluminum cooled until the vapor layer under the droplet failed at $T_- < 100^\circ\text{C}$ (Video S1). The failure temperature, T_- , was highly dependant on drop size. The droplet in video S1 existed on the surface well below boiling, yet larger drops are expected to fail at higher temperatures due to the hydrodynamic stability of the vapor layer [4].

VI. COOLING EXPERIMENTS

In order to measure d versus T_s , we performed experiments where the upper electrode was heated well above T_+ , to 500-600 $^\circ\text{C}$, before immersing it in the liquid bath. The initial temperature of the bath was set at $T_i = 75^\circ\text{C}$. Upon lowering the upper electrode into the bath at a fixed distance from the bottom electrode, a vapor layer instantly formed around the tip with no liquid-solid contact. We used the same sampling rate as in the hysteresis experiments, described above. We measured d , T_s , and T_i every second until $T_s = T_-$ at failure.

We tested 3 metals with varying thermal conductivity, titanium (7 W/m·K), brass (115 W/m·K), and copper (390 W/m·K). Each rod was polished with micron-scale lapping compound, resulting in a reflective finish. The copper and brass rods were electroplated with nickel to inhibit surface corrosion during rapid heating and cooling over many experiments in salt water. For each metal, we used NaCl concentrations from 0-0.6 M, where the upper

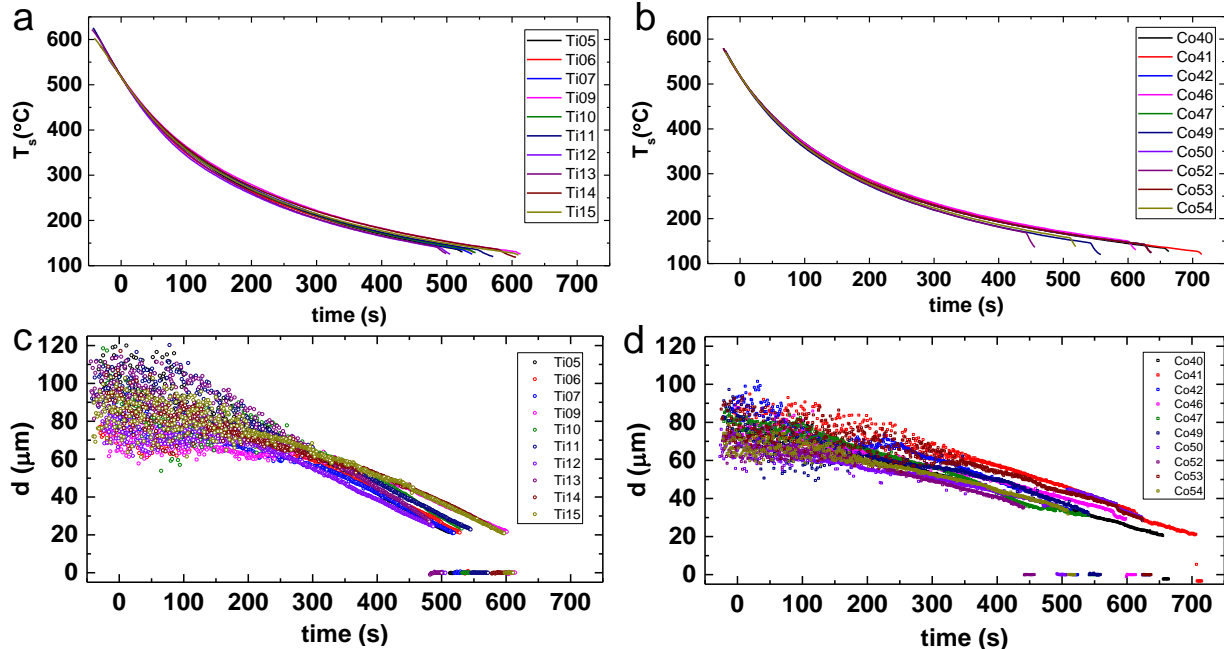


FIG. S5. Series of individual experiments showing the surface temperature T_s versus time for titanium (a) and copper (c), and the thickness d versus time for titanium (c) and copper (d). All data have been shifted in time so that $T_s = 520^\circ\text{C}$ at the origin. The legend denote different individual experiments.

range roughly corresponds to the concentration of NaCl in sea water. Figure. S5 shows a number of single experiments for titanium, (a) and (c), and copper, (b) and (d). All the data in these graphs have been shifted in time so that $T_s = 520^\circ\text{C}$ at the origin. The salt concentration varied between the different experiments listed in the legend.

Figure S5a-b show that on average, it took longer for the copper rod to cool under the same conditions as the titanium. This is expected since the heat capacity of copper is larger than titanium. There is little variation between experiments, but this did not correlate with salt concentration (Fig. 3c in the main text). Most importantly, the cooling curves show that on average $T_s \approx 140^\circ\text{C}$ for both metals. Figure S5c-d show the corresponding vapor layer thickness as functions of time. The noise is most significant at large d since the corresponding capacitance (impedance) is much smaller (larger). Runs for each metal tend to follow the same slope as the metal cools. However, the slopes are very different for the two metals, since d is most dependent on T_s (Fig. 3a in the main text). We also note that the thickness at failure (d_c) tends to vary more for the copper than the titanium, perhaps because the copper is cooling down more slowly and thus spends more time at the lower temperatures (smaller d).

VII. COMSOL VAPOR LAYER SIMULATIONS

The evaporation, thermodynamics, and hydrodynamics of the vapor layer, solid, and liquid phases result in a complex coupled system with dynamics on small length scales. In order to provide some insight into our experimental results, we simulated a two-dimensional Leidenfrost system around a semicircle using the laminar flow, phase fields, and heat transfer modules in COMSOL multi-physics 5.3a [1]. The simulation uses real properties of copper, pure liquid water, and water vapor. A profile from a typical simulation is shown in Fig. S6a, right before the collapse of the vapor layer.

This simulation is based off a 2D pot boiling tutorial by DOJO Research & Consulting (https://youtu.be/Awwza_v27EA). The evaporation parameters and heat transfer coefficients in the fluid are the same, but we adapted the system geometry to model our experiments. We introduced an inflow of fluid from the bottom to maintain an approximately constant water level. Liquid evaporates and exits through the top of the simulation domain, which is held at constant pressure. We also added heat transfer in the solid.

The 2D simulation space is a 20×12 mm rectangular container with a semicircle metal object of radius 8 mm (Fig. S6a). The dark blue represents the liquid water phase and the white space between the hemisphere and water surface is water vapor. The surface of the water marks the 80% liquid water phase from the phase field

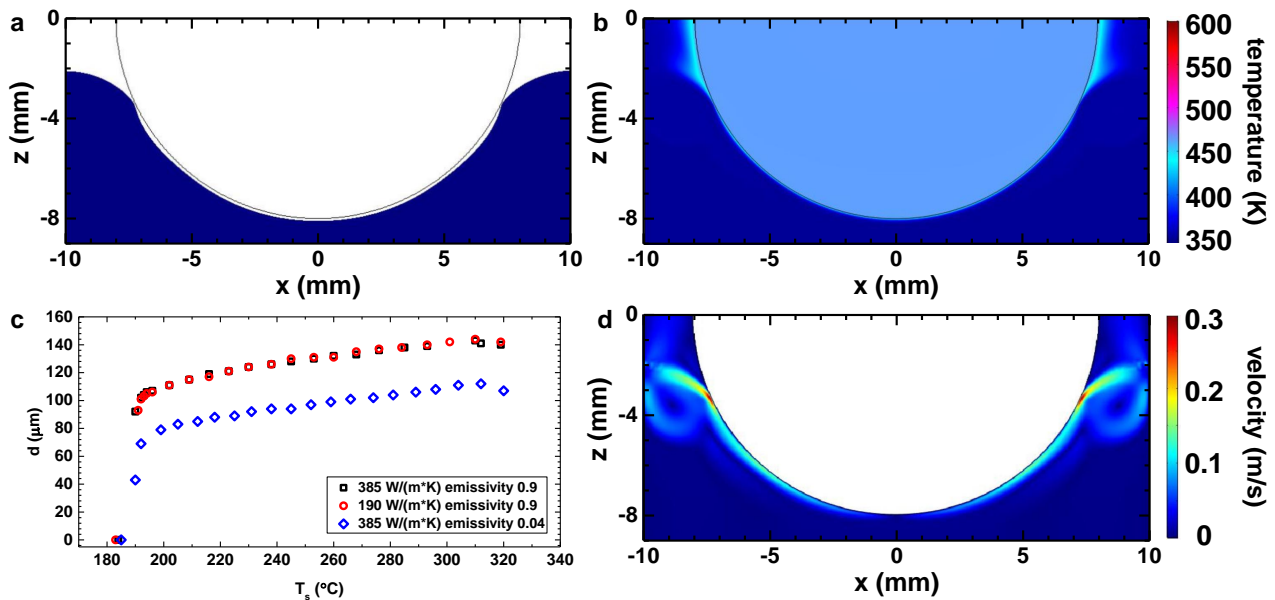


FIG. S6. (a) Model output showing the profile of a 2D simulation where the water line represents 80% in the phase field. (b) The temperature profile from the simulation, where the surface of the heated object is ≈ 460 K right before collapse of the vapor layer. (c) The thickness at the bottom tip of the heated object as a function of T_s as the object cools down. Failure of the vapor layer occurs at $T_- \approx 190^\circ\text{C}$. (d) The magnitude of the velocity field in both phases right before collapse, showing a peak at ≈ 0.3 m/s near the point of failure.

module. The metal is initialized at 600 K, while the water and water vapor are 350 K. Initially, the simulation space is filled by a uniform liquid water inflow at the base with velocity 0.0025 m/s. As the liquid approaches the solid a Leidenfrost vapor layer forms due to the rapid evaporation of the liquid near the metal surface.

Heat transferred from the metal to the liquid causes evaporation and heating of the surrounding water vapor. The vapor can escape the top of the simulation space through a fixed 1 atm pressure boundary. The simulation examines each piece of mesh and uses the local temperature to determine if that section should evaporate or condense. It then calculates the energy cost of the phase transition and adjusts the temperature appropriately. However, we found that mass conservation was not strictly obeyed, which is a common problem in phase field modeling of two components with vastly different densities.

As the simulation evolves, the metal cools and the vapor layer thins until $T_s = T_-$, which marks the failure of the vapor layer just as in experiments. In simulations, $T_- \approx 190^\circ\text{C}$ (Fig. S6c). Figure S6a, S6b, and S6d show the last frame of the simulation before collapse for a semi-circle with the properties of copper: thermal conductivity = 385 W/m·K, density = 8,940 kg/m⁻³, and heat capacity = 385 J/kg·K. Figure S6b shows the temperature throughout the container and S6d shows the velocity in the fluid, showing a sharp peak around 0.3 m/s at the point of minimum thickness.

The exact value T_- is nearly independent of the thermal conductivity of the semi-circle, but depends on the

total heat transfer. Figure S6c shows d versus T_s , in analogy with Fig. 3a in the main text, for 3 different simulations. In simulations d is measured from the bottom of the semi-circle to the 80% line. The red points are from the simulation described above, using a realistic surface emissivity = 0.9 for metal that has been slightly oxidized by heating. The black points show an identical simulation except the thermal conductivity was set to 190 W/m·K. The data is nearly indistinguishable, in agreement with Fig. 3a. The blue points use the real properties of copper, but with a surface emissivity of 0.04, which would represent an optically polished metal surface. This shifts d to lower values since the total heat transferred to the liquid is partially dependent on radiative coupling, and the surface emits and absorbs less radiation. However, the vapor layer seems to collapse at the same value of $T_- \approx 190^\circ\text{C}$ for all simulations.

The simulation agrees qualitatively with the experiments. The vapor layer thickness decreases as the metal cools, and there is a minimum temperature, T_- , below which a vapor layer cannot exist. This limit is not affected by thermal properties of the metal. Looking at the profile in Fig. S6a, we can make inferences about the driving mechanism for collapse. A full time evolution of the simulation is shown in video S4, corresponding to Fig. S6 (red points in panel c). The vapor layer profile includes a thin region similar to the “neck region” observed under Leidenfrost drops and drops levitated by an airflow [4–8]. The velocity is maximum at this point, and this is also where the vapor layer fails. Prior to collapse, the point of minimum thickness is never at the tip, which

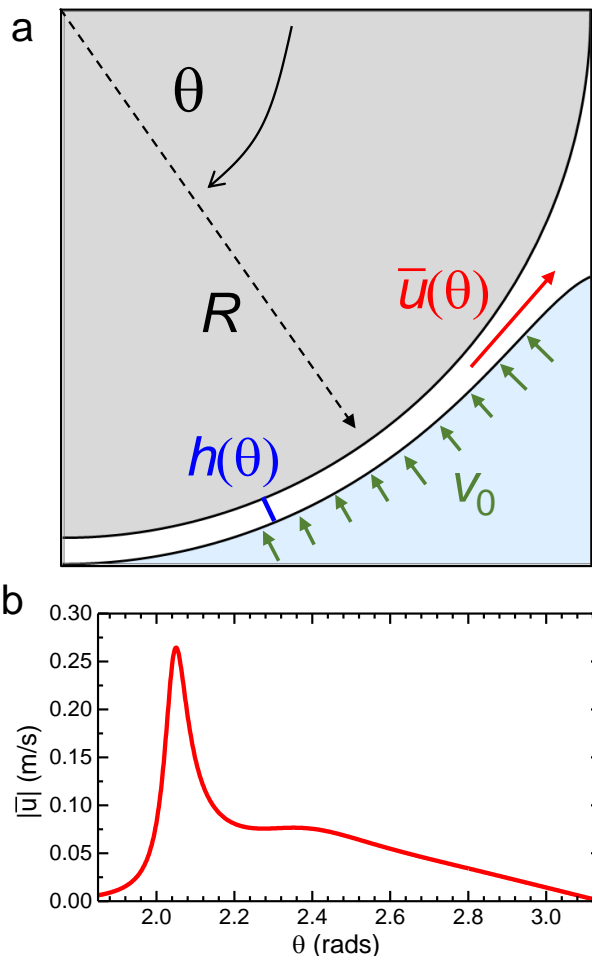


FIG. S7. (a) Schematic of the geometry used in the lubricating flow. The local thin film thickness is $h(\theta)$, and the depth-averaged velocity is \bar{u} . The layer is fed by a uniform gas flow from the liquid-vapor surface with velocity $v_0 \ll \bar{u}$. (b) Solution of Eqs. 12 and 13 for \bar{u} with $v_0 = 0.001$ m/s assuming a water-vapor interface at the boiling point. The corresponding solution for h is shown in Fig. 4c in the main text. The boundary conditions are $h(\pi) = 40.32$ μm , $h'(\pi) = 0$, and $h''(\pi) = 8.4$ μm .

may explain why we typically see the initial liquid-solid contact away from the tip in experiments (Fig. 2b in the main text). These results suggest that the hydrodynamics of the vapor layer alone may determine the point of failure and the equilibrium thickness.

VIII. LUBRICATION APPROXIMATION

In order to disentangle thermodynamic effects from purely hydrodynamic ones, we employed a simple model based on lubricating flow in a viscous vapor layer. Nearly identical models have been used for the air flow under a levitated drop [4, 7, 8]. In particular, predictions from Snoeijer et al. [4] show excellent agreement with ex-

periments of Leidenfrost drops [5]. The lubrication approximation balances the leading order pressure gradient terms driving the tangential flow in the vapor layer, with a conservation of mass in the flow. For our model, both the fluid interface and the solid material are considered motionless. This is valid if the velocity in the fluid is considerably less than in the thin, vapor layer. Figure. S6d supports this assumption.

The Reynolds number, Re , in the vapor layer is also assumed to be small enough so that inertia can be safely ignored. Estimates for the flow beneath centimeter-scale droplets suggest that $Re \lesssim 0.3$ [9], so this assumption is reasonable for our simple model. Since we are not explicitly considering evaporation, we assume that there is a constant flow of gas that feeds the vapor layer at velocity v_0 . We only consider the flow around the lower part of a hemisphere immersed in a liquid, and use axisymmetric spherical coordinates so that the tip of the hemisphere (with radius R) corresponds to $\theta = \pi$ (Fig. S7a). Both the film thickness, $h(\theta)$, and the depth-averaged velocity, $\bar{u}(\theta)$, vary with the angular coordinate. We will assume that $h \ll R$, and that $h' \ll R$, where prime denotes differentiation with respect to θ . This means that the film is thin and that its thickness varies slowly along the edge of the hemisphere.

With these assumptions, there are two differential equations that describe the steady profiles of h and $\bar{u}(\theta)$:

$$h\bar{u} \sin \theta = -Rv_0(1 + \cos \theta), \quad (12)$$

$$12\eta \frac{\bar{u}}{h^2} = \frac{1}{R} \frac{d}{d\theta} \left[\rho_l g (R + h) \cos \theta + \gamma \kappa \right]. \quad (13)$$

The first equation comes from mass conservation of the gas in the vapor layer, assuming that $\bar{u}(\pi) = 0$ from symmetry considerations. The mass continuity in the vapor layer at θ results from the integrated amount of gas entering the vapor layer, starting from $\theta = \pi$. The second equation balances the pressure gradient necessary to drive the flow \bar{u} in the lubricating vapor layer with the pressure gradient determined by hydrostatic (gravitational) forces and variations in the Laplace pressure. The variable $\kappa = \kappa(\theta)$ is the total curvature of the interface, and can be calculated by taking the divergence of the normal vector to the liquid-vapor interface:

$$\kappa = \vec{\nabla} \cdot \hat{\mathbf{n}}, \quad (14)$$

$$\hat{\mathbf{n}} = \left(-\hat{\mathbf{r}} + \frac{h'}{R+h} \hat{\boldsymbol{\theta}} \right) \left(1 + \frac{h'^2}{(R+h)^2} \right)^{-1/2}, \quad (15)$$

where the spherical coordinate r is evaluated at $R + h$ after differentiation. Here we have kept the full curvature with no approximations in order to correctly model the shape of the interface all the way to the boundary.

Equation 12 can be solved directly for \bar{u} and inserted into Eq. 13, resulting in a third-order differential equation for $h(\theta)$. For a given gas input velocity (v_0), we choose initial values of $h(\pi)$ and $h''(\pi)$ since $h'(\pi) = 0$ by axisymmetry. We then solve the resulting equation for $h(\theta)$ until we match the conditions at the boundary (i.e.,

$x = 10$ mm in Fig. 4b in the main text). We match the height of the liquid level at the boundary, and require that $h' = (R + h) \cot \theta$, which corresponds to the requirement that the normal of the interface points in the z direction. Using the properties for water and steam at the boiling point ($\rho_l = 959$ kg/m³, $\gamma = 59$ mN/m, $\eta = 1.3 \times 10^{-5}$ Pa·s), and using $v_0 = 0.001$ m/s, we illustrate a steady solution where $h(\pi) = 40.32$ μ m in Fig. 4c in the main text. The corresponding velocity, \bar{u} , is shown in Fig. S7b. The peak at $|\bar{u}| \approx 0.25$ m/s corresponds to the minimum in h , and agrees very well with the velocity from the full COMSOL simulation (Fig. S6d).

There are a few things to note about the solutions. First, the solution is technically not valid when $h \sim R$. For boundaries which are not too far from the solid edge

at R , this is acceptable [7], but for far-field boundaries the solution would need to be matched to an outer solution for the liquid-vapor interface. Second, these are steady solutions, so there are no dynamics. This means that for a given v_0 and set of boundary conditions, a solution may not exist. In fact, the structure of the branches where solutions exist is quite complicated, as may be expected from similar problems considering the lubricating flow under droplets [7, 8]. In reality, a vapor layer may exist for a given thickness and boundary conditions in the experiments, but it will fluctuate in time. Periods of quiescent behavior in the experiment correspond to regimes where steady solutions of the lubricating vapor layer exist. The problem is richer than what is presented here, yet a detailed examination of the solution branches and their stability is left for future work.

-
- [1] COMSOL Multiphysics®, v. 5.3. COMSOL AB, Stockholm, Sweden (2020).
- [2] J. D. Paulsen, J. C. Burton, and S. R. Nagel, Viscous to inertial crossover in liquid drop coalescence, PRL **106**, 114501 (2011).
- [3] M. Khademi and D. P. J. Barz, Structure of the electrical double layer revisited: Electrode capacitance in aqueous solutions, Langmuir **36**, 4250 (2020).
- [4] J. H. Snoeijer, P. Brunet, and J. Eggers, Maximum size of drops levitated by an air cushion, Phys. Rev. E **79**, 053011 (036307).
- [5] J. C. Burton, A. L. Sharpe, R. C. A. van der Veen, A. Franco, and S. R. Nagel, Geometry of the vapor layer under a leidenfrost drop, Phys. Rev. Lett. **109**, 074301 (2012).
- [6] T. A. Caswell, Dynamics of the vapor layer below a leidenfrost drop, Physical Review E **90**, 013014 (2014).
- [7] J. R. Lister, A. B. Thompson, A. Perriot, and L. Duchemin, Shape and stability of axisymmetric levitated viscous drops, J. Fluid Mech. **617**, 167 (2008).
- [8] L. Duchemin, J. R. Lister, and U. Lange, Static shapes of levitated viscous drops, J. Fluid Mech. **533**, 161 (2005).
- [9] X. Ma, J. Liétor-Santos, and J. C. Burton, Star-shaped oscillations of leidenfrost drops, Physical Review Fluids **2**, 031602(R) (2017).